

Post-print of: Golvano-Escobar, Irati et al. "Electrodeposition of sizeable and compositionally tunable rhodium-iron nanoparticles and their activity toward hydrogen evolution reaction" in ***Electrochimica acta***, Vol. 194 (Marzo 2016) , p. 263-275. The final version is available at DOI 10.1016/j.electacta.2016.02.112

Electrodeposition of sizeable and compositionally tunable rhodium-iron nanoparticles and their activity toward hydrogen evolution reaction

Irati Golvano-Escobar,^a Santiago Suriñach,^a Maria Dolors Baró,^a Salvador Pané,^{b,} Jordi Sort,^{c,*} and Eva Pellicer^{a,*}*

^aDepartament de Física, Facultat de Ciències, Universitat Autònoma de Barcelona, E-08193 Bellaterra, Spain.

^bMulti-Scale Robotics Lab (MSRL), Institute of Robotics & Intelligent Systems (IRIS), ETH Zürich, Zürich 8092, Switzerland.

^cInstitució Catalana de Recerca i Estudis Avançats (ICREA) and Departament de Física, Universitat Autònoma de Barcelona, E-08193 Bellaterra, Spain.

* vidalp@ethz.ch

* Jordi.Sort@uab.cat

* Eva.Pellicer@uab.cat

Abstract

Rh-Fe nanoparticles (NPs) with variable Rh/Fe ratios have been obtained by direct current electrodeposition onto Au-metalized Si/Ti substrates from an electrolyte containing Rh(III) and Fe(III) chloride salts. NP mean diameter could be varied in the range of 20-80 nm by playing with the applied current density ($-j = 0.5\text{-}2\text{ mA cm}^{-2}$) and deposition times ($t = 200\text{-}3200\text{ s}$). NPs were very well adhered to the substrate and became progressively enriched in Fe as the absolute value of the current density increased. X-ray photoelectron spectroscopy analyses revealed that the NPs are mostly metallic. The oxygen signal detected at surface level is relatively high but reduces down to less than 1 at% after 1 min Ar ions sputtering. The as-deposited Rh-Fe NPs are active toward hydrogen evolution reaction in alkaline medium. Different values of the onset potential for water reduction have been observed depending on the j and t values applied for NPs growth. Cycling stability tests reveal that NPs do not suffer from excessive deterioration of their electrocatalytic activity with time.

Keywords: nanoparticles; electrodeposition; hydrogen evolution reaction; rhodium-iron.

1. Introduction

Nanoparticles (NPs) exhibit a wealth of physical and chemical properties associated with their crystal structure, chemical and electrochemical reactivity or electrical and magnetic properties at the nanoscale [1]. For this reason, NPs have become the cornerstone for the development of next generation of sensing, energy conversion, electronic, optoelectronic, and magnetic devices [2-4]. Among the synthesis methods to produce substrate-supported

NPs, electrochemical deposition is one of the least expensive, highly productive and readily available methods [5-7] Electrodeposition enables not only directly growing the NPs onto the substrate, but also to tune on-demand the NPs composition, the crystallographic structure, the size, and the shape by playing with the electrodeposition parameters [8-10].

Rhodium (Rh) is a precious transition metal with intriguing properties including chemical inertness towards mineral acids, outstanding catalytic properties for a variety of organic transformations [11-14] and electrocatalytic properties [15]. For those reasons, Rh has been broadly employed in fuel cells, solar energy conversion devices and for environmental remediation [16].

However, one of the main drawbacks associated with Rh is its high price, which makes it necessary to partially replace Rh by more abundant and less expensive elements. Iron (Fe), as one of the most earth-abundant elements, is a suitable candidate. For example, Haider and co-workers synthesized Fe-promoted Rh catalysts by incipient wetness impregnation. They showed that the addition of Fe to the catalyst significantly improved the catalytic activity and the selectivity of the material toward ethanol and other oxygen-containing compounds [17]. Likewise, Nakamura et al. synthesized bimetallic Rh/Fe NPs by stepwise complexation for the hydrogenation of olefins and nitroarenes. They showed improved catalytic performance toward these hydrogenation reactions, under relatively mild conditions, in comparison with previously reported hydrogenation reactions using pure Rh NPs [18].

Hydrogen evolution reaction (HER) is a cathodic reaction in the electrolysis of water that allows producing hydrogen as a key energy carrier [19]. HER is of uttermost importance in electrochemical energy conversion devices such as electrolyzers, fuel cells and solar

hydrogen devices [20]. Although Rh cannot compete with Pt in terms of HER in alkaline medium, Rh still shows a reasonable activity [21,22]. For example, Smiljanic et al. found that bimetallic catalysts composed of Rh nanoislands on Pt exhibited enhanced HER performance with respect to bare Pt [23]. Meanwhile, Fe and its compounds (e.g. hydro(oxy)oxides) have been developed as highly efficient HER electrocatalysts under acidic or alkaline conditions [24,25]. Due to their large surface area, NPs are expected to outperform thin films in HER.

The present work aims to demonstrate that Rh- and Fe-containing NPs can be successfully prepared by electrodeposition. Although there are studies on either the electrodeposition of Rh [26,27] or Fe [28], little attention has been paid to the codeposition of these two elements [29,30], and certainly not in the form of NPs. It will be shown that the here-presented deposition scheme renders Rh-Fe NPs whose chemical composition and size can be adjusted by simply changing the current density and deposition time. The HER characteristics of the deposited NPs have been investigated in alkaline media and the trends observed have been outlined.

2. Experimental

2.1 Electrochemical synthesis of Rh-Fe NPs

NPs were synthesized by direct current electrodeposition in a thermostated three-electrode cell using a PGSTAT 302N Autolab potentiostat/galvanostat (Ecochemie). Au (125 nm) / Ti (25 nm) coated Si/SiO₂ chips were used as cathodes (working area 0.25 cm²). A double junction Ag|AgCl (E=+0.210 V/SHE) reference electrode (Metrohm AG) was used with 3 M KCl inner solution and interchangeable outer solution made of 1 M NaCl. A platinum spiral served as counter electrode. The electrolyte consisted of 0.5 mM

$\text{Cl}_6\text{Na}_3\text{Rh}$, 0.01 M FeCl_3 , 0.05 M glycine and 0.05 M NaCl. The pH of the as-prepared electrolyte was 2.4 and it was kept for the electrodeposition experiments. Solutions were prepared from analytical grade reagents and Milipore MilliQ water. Prior to deposition, the Au surface was first degreased with acetone followed by washing in isopropyl alcohol and water. Before each deposition, the electrolyte was de-aerated with nitrogen gas. Deposition was conducted galvanostatically, by applying a constant current density in the range from -0.5 to -4 mA cm^{-2} , under mild stirring (200 rpm) using a magnetic stirrer bar. After deposition, the samples were thoroughly rinsed in water followed by 1 min sonication in methanol and stored in a low pressure container to minimize oxidation of the NPs.

2.2 Characterization

The morphology, size and composition of the Rh-Fe NPs were characterized with a Zeiss Merlin field emission scanning electron microscope (FE-SEM) equipped with an energy dispersive X-ray (EDX) detector. At least two replicas per condition were analysed. In order to determine the mean NP size, 100 NPs were counted per condition using the ImageJ software. The crystallographic structure of the electrodeposited NPs was studied by transmission electron microscopy (TEM) in a JEOL JEM-2011 microscope operated at 200 kV. Scanning transmission electron microscopy (STEM)-EDX line profile analyses were performed on a Tecnai F20 microscope. The NPs were scratched from the Au/Ti/Si substrate with an agate mortar. Complementary inductively coupled plasma mass spectroscopy (ICP-MS) analyses were conducted to determine the metal content. To ensure Rh dissolution, aqua regia was used. Measurements were done on a 7500ce spectrometer from Agilent Technologies. The oxidation state of the NPs was assessed by X-ray photoelectron spectroscopy (XPS). XPS analyses were carried out at room

temperature on a PHI 5500 Multitechnique System (from Physical Electronics) spectrometer, equipped with a monochromatic X-ray source ($K_{\alpha Al}$ line with energy of 1486.6 eV and 350 W), placed perpendicular to the analyser axis and calibrated using $3d^{5/2}$ line of Ag with a full width at half maximum (FWHM) of 0.8 eV. The analysed area was a 0.8 mm diameter disk surface for each sample. Charging effects were corrected by referencing the binding energies to that of the adventitious C1s line at 284.5 eV.

2.3 Electrocatalytic activity towards HER

The electrocatalytic activity of the NPs towards HER in alkaline medium was also explored in a conventional three-electrode cell, using a Ag|AgCl (3M KCl) and a Pt spiral as reference and counter electrodes, respectively. The NPs previously deposited on Si/Ti/Au substrate served as the working electrode. Linear sweep voltammetry (LSV) and cyclic voltammetry (CV) measurements were conducted under stagnant conditions in de-aerated 0.1 M NaOH solution at 25 °C. The potential was scanned between -0.5 V and -1.5 V at a scan rate of 50 mV s^{-1} . The potential was held at -0.4 V during 5 min in LSV and in the first CV scan before sweeping the potential toward cathodic values. The stability of the catalysts was assessed by both cycling tests and chronoamperometry.

3. Results and discussion

3.1 Morphology and structure of the Rh-Fe NPs

A series of NPs with varying size and composition were prepared on Au/Ti/Si substrates by applying the following current densities: -0.5 , -2 , and -4 mA cm^{-2} . These values were chosen from cyclic voltammetry (CV) experiments (not shown).

In order to prevent the formation of continuous films, an Fe(III) salt was selected. It is known that the current efficiency of Fe(III) electrolytes is typically very low so that long deposition times are needed to obtain films [31]. Moreover the standard reduction potential of Fe (III) is -0.04 V whereas that of Fe (II) is -0.41 V. Taking into account that the standard reduction potential for Rh (III) is +0.44 V, the co-deposition of Fe and Rh from Fe (III) salts should be in principle more favourable. The E-t curves recorded during deposition are shown in Fig. 1. The potential remained fairly constant soon after deposition started. Rounded NPs at relatively moderate or high coverage were achieved in all conditions. Fig. 2 shows SEM images of the NPs grown at current densities of -0.5 , -2 , and -4 mA cm^{-2} . At fixed deposition charge ($Q = 800 \text{ mC cm}^{-2}$), the mean NP size decreased with the current density (cf. Fig. 2b and 2f), indicating a reduction of the current efficiency of the process.

For a fixed current density, finer NPs were obtained for shorter deposition times. Fig. 3a shows that NPs of $\sim 60 \text{ nm}$ in diameter are obtained at -0.5 mA cm^{-2} for 3200 s of deposition time. At half deposition time, the mean NP diameter decreases to $\sim 40 \text{ nm}$ (Fig. 3b). With further decrease of the deposition time (800 s) the NPs get apparently even smaller (Fig. 3c). Fig. S1 and S2 show FE-SEM images of NPs grown at -2 mA cm^{-2} and different deposition times as well. The trend is clear when comparing extreme deposition times (see Table 1), but fluctuations were noticed for intermediate deposition times due to the uncertainty of the image analysis for particle sizing and the inherent complexity of the deposition process. The histograms for all deposition conditions are shown in the Supporting Information (Fig. S3). Even though monosized NPs are not achieved, which is probably the most challenging and not yet solved issue related to NPs growth by electrodeposition, relatively narrow particle size distributions are obtained up to 1600 s

irrespective of the current density. At long deposition times (3200 s) the size distributions become broader as NPs tend to coalesce.

EDX analyses revealed the presence of Rh and Fe elements, together with Au (coming from the substrate), C and O (Fig. 4). Table 2 lists the amount of Fe (in at%) detected in NPs deposited within the selected experimental conditions. Although these values should be taken with care due to the small volume of deposited material, trends show that the Rh content decreases with an increase in the absolute value of current density. At a fixed current density, variations in the chemical composition with the deposition time were also noticed in spite of stirring the solution. At current densities of -0.5 and -2 mA cm^{-2} and at a fixed time, the composition of the NPs remained the same. Upon increasing of current density, the Fe content increases. Complementary ICP-MS analyses were in concordance with the observed trends. This is in agreement with some observations made by Tabakovic et al. in their studies of electrodeposited CoFeRh alloy films [32]. In their work, similar trends were observed regarding the Fe and Rh content with the applied current density. Since Rh is nobler than Fe, the growth of Rh-rich deposits is in principle expected at low overpotentials (or current densities). Likewise, Fe discharge is to be favoured at higher overpotentials (or current densities). It is conjectured that Rh(III) discharge is mainly controlled by diffusion [33]. Other studies suggest that Rh growth proceeds via mixed kinetics, charge transfer and diffusion [34]. Fe is likely activation-controlled within the deposition potentials range used in this study. As a result the NPs become gradually enriched in Fe upon making the overpotential more negative.

XPS measurements were performed in order to gain further insight on the chemical composition of the NPs. Measurements were carried out both before and after Ar ions sputtering for 1 min. Fig. 5a displays the survey spectrum (taken before Ar sputtering) of

NPs electrodeposited at -0.5 mA cm^{-2} for 1600s. The spectrum shows the presence of Rh, Fe, O, C, N and Cl elements. The latter (C, N and Cl) are appended to surface contamination. Nevertheless, C is also a typical impurity in electrodeposited metals and alloys [35]. In our case, glycine decomposition could well be a source of C. The small peak of chlorine can be well attributed to the electrolyte residue remaining after samples' washing. The corresponding Rh3d, Fe2p and O1s core-level electronic transitions are given in Fig. 5b. Regarding Rh3d signal, the $3d_{5/2}$ and $3d_{3/2}$ doublet peaks located at 307.1 and 311.9 eV, respectively, correspond to the zero oxidation state of Rh ($\Delta_{\text{metal}} = 4.8 \text{ eV}$). Besides, they show the typical asymmetric peak shape for Rh metal [36]. The higher binding energy shoulders located at 309.7 and 314.2 eV can be attributed to Rh(III). The presence of Rh_2O_3 in the NPs is not unexpected. Actually, Rh_2O_3 was detected by XPS in electrodeposited Rh films from $\text{RhCl}_3\text{-NH}_4\text{Cl}$ solution at $\text{pH} = 4$ [37]. Concerning the Fe2p core level XPS spectrum, the position of $\text{Fe}2p_{3/2}$ peak (711.7 eV) and $\text{Fe}2p_{1/2}$ peak (725.3 eV) are characteristics of Fe^{2+} [38]. The shoulder in between could be assigned to metallic Fe. The O1s spectrum shows a relatively intense double peak with two maxima at 532 eV, typical for metal hydroxides (M_xOH_y) and at 530 eV, distinctive for metal oxides (M_xO_y) (Fig. 5d). Tabakovic et al. also noticed relatively high contents of oxygen (32 at%) in electrodeposited Rh films [37].

After 1 min Ar ions sputtering, the O signal in the corresponding XPS survey pattern and core-level transition detail is clearly reduced (Fig. 6a and 6b). Interestingly, the Rh3d signal only shows the doublet assigned to Rh metal (Fig. 6b). Likewise, the peaks assigned to zero-valent Fe (707.6 eV for $2p_{3/2}$ and 720.4 eV for $2p_{1/2}$) [37] clearly emerge. Nevertheless, care should be taken when analysing the oxidation state of iron oxides since reduction of iron oxidation state by Ar-ions bombardment has been observed, in

particular from Fe^{3+} to Fe^{2+} [39]. Full reduction of Fe^{2+} toward Fe^0 upon Ar-ions irradiation is less probable and indeed STEM-EDX analyses indicate that the oxygen signal is rather low.

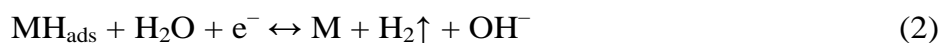
Table 3 shows the Rh, Fe and O amounts (in at%) for NPs electrodeposited at -0.5 mA cm^{-2} for 1600s determined by XPS before and after Ar ions sputtering. It is clear that the oxygen signal greatly diminishes down to less than 1 at% after Ar ions sputtering. Similar results were obtained for other Rh-Fe NPs. This result suggests that the NPs have oxidized surfaces. Nevertheless, assuming a sputter rate of about $7\text{-}10 \text{ nm min}^{-1}$, the results indicate that the oxidized shell is indeed very thin and hence, the NPs are mostly metallic. Bearing in mind the nobility of Rh, the detection of Rh(III) by XPS before sputtering suggests that Rh oxides already form during deposition, in agreement with Tabakovic et al. [37] Concerning Fe, oxides could also form during electrodeposition as for Rh or show afterwards. Fe is prone to oxidation on standing in air, a phenomenon that is exacerbated in nanoscale materials [40]. Notice that the samples were not stored in high vacuum. Yet, the NPs displayed similar levels of oxygen both in the as-deposited state and after storage for a few days. Therefore eventual passivation likely takes place immediately after electrodeposition.

HRTEM was used to retrieve structural information of the NPs. It is worth mentioning that the NPs were very well adhered to the substrate since ultrasonication did not cause detachment of the NPs even for long sonication times. Fig. 7a shows most probably part of an aggregate of a few NPs. A close-up image reveals that the NP is composed of small crystallites of less than 5 nm (Fig. 7b). An extremely thin (ca. 1 nm-thick) layer is seen at the uttermost surface. The lattice fringes are evident, which demonstrates that the NPs are highly crystalline. Additional HRTEM images are shown in the Supporting Information

(Figure S4). The selected area electron diffraction (SAED) pattern, taken on an aggregate of NPs (Fig. 7c), shows spotty rings. The corresponding interplanar distances match those of (111), (200), (220) and (311) planes of cubic metallic Rh (PCPDF 05-0685). Some distances are also consistent with iron and rhodium oxides (Rh₂O₃), in agreement with XPS results. In order to determine the Fe distribution within the NPs, STEM-EDX line scan analyses were performed. Representative results are provided in Figure 8. Fe was found to be homogeneously distributed within the NPs. Moreover, a uniform distribution was also disclosed when analysing the single crystallites (about 3-4 nm in size) which compose the bimetallic NPs.

3.2 Electrocatalytic activity

The deposited NPs were expected to be suitable candidates for HER not only because of their chemical composition but also because of the high surface area. Fig. 9 shows the LSV curves recorded in Ar-purged NaOH 0.1 M at a sweeping rate of 50 mV s⁻¹ for different Rh-Fe NPs. NPs featuring different Fe contents (between 16 and 36 at% Fe) obtained at deposition times up to 1600 s were selected. For comparison, the LSV curve of the bare Si/Ti/Au substrate is shown. While the Au surface shows almost negligible catalytic activity, the NPs are active toward HER. A large density of hydrogen bubbles emerging from the Rh-Fe NPs was visible at naked eye when the potential passed by -1.2 V toward the negative direction. There is an agreement that HER mechanism in alkaline media consists of three steps [19]:



The first reaction (Eq. 1), which involves the electroreduction of water into adsorbed hydrogen, is termed Volmer reaction. This is followed by the electrochemical hydrogen desorption (Eq. 2) known as Heyrovsky reaction, or the chemical hydrogen desorption (Eq. 3) known as Tafel reaction. The Heyrovsky and Tafel reactions proceed either alternatively or simultaneously. Note that although M designates the metal, both metallic and oxidized forms of Fe and Rh would contribute. Since HER takes place at the surface of the NPs, the role of a partially oxidized shell coating the NPs cannot be neglected.

Slightly different onset potentials for H₂O reduction toward H₂ were observed depending on the electrodeposition conditions used to grow the NPs. The sample obtained at -0.5 mA cm^{-2} for 1600 s exhibits the best performance. The corresponding onset potential for HER is -0.93 V , whereas the rest of the samples show more negative values (Table 4). Interestingly, at a potential of -1.2 V the corresponding current density is not far away to the value reported for polycrystalline Pt ($j \sim 13 \text{ mA cm}^{-2}$) tested in 0.1 M NaOH , although at a lower scan rate of 10 mV s^{-1} [21]. The outperforming NPs are Rh-rich (19 at% Fe as listed in Table 2) and show moderate substrate coverage. However, since changes in composition, nanoparticle size and coverage degree occur simultaneously with varying the current density during the electrodeposition step, it is difficult to draw straightforward conclusions. Nevertheless, upon carefully examining the LSV curves, some other interesting features emerge. For example, although the electrocatalytic activity of the NPs deposited at -4 mA cm^{-2} for 800 s diminishes compared to that of NPs deposited at -0.5 mA cm^{-2} for 1600 s, its Fe content is much higher (36 at%). Therefore, there is a trade-off between the slight loss in electrocatalytic activity and the partial replacement of pricy Rh by cheaper and more abundant Fe.

For the aim of comparison pure Rh and Fe materials were electrodeposited from Fe-free and Rh-free electrolytes, respectively. Although baths were similar to that of Rh-Fe, both the coverage degree and the morphology were distinct (Fig. 10), which indicates that there is a synergistic effect when Rh and Fe are electrodeposited together. Pure Rh can be deposited as NPs but their surface looks much rougher as reported by Kibler et al. [41]. These authors showed that electrodeposition of Rh at low overpotentials start with the formation of a bilayer and that further deposition proceeds via a Stranski-Krastanov growth mode, accompanied by a strong roughening of the surface. Moreover, at a current density of -0.5 mA cm^{-2} and 1600 s of deposition time the mean size is larger than that of Rh-Fe NPs grown under the same conditions (Figure 3(b)). Pure Fe did not form NPs but, instead, a highly porous film developed onto the electrode. In this case it was necessary to apply a current density of -4 mA cm^{-2} in order to get some deposition. Interestingly, both pure Rh and Fe are less active than most of the Rh-Fe NPs. The corresponding LSV curves are compared with that of the outperforming Rh-Fe NPs in Figure 11.

Bimetallic systems often show improved electrocatalytic activity compared to their pure counterparts. Synergisms, modification of electronic/chemical properties or geometric considerations have been advocated as responsible for the improvement. Introducing another element into the lattice of a given metal is an effective way to modify its electronic/chemical properties by creating a bimetallic surface through: i) formation of heteroatom bonds leading to a ligand effect, and ii) alteration of the average metal-metal bond length, resulting in a strain (e.g. compressive or tensile) effect [20]. Besides the aforementioned changes in morphology (i.e., geometric features), the formation of a bimetallic surface likely gives rise to modifications of the electronic properties of both Rh and Fe metals and alters the average Rh-Rh metal bond. This might partially explain the observed enhancement of the HER activity.

In order to examine the stability of the catalysts, the Rh-Fe NPs were subjected to 50 CV cycles in 0.1 M NaOH electrolyte within the potential range from -0.5 V to -1.5 V (Fig. 12 and Fig. S5-S9). Fig. 12 shows the 1st, 5th, 10th, 20th and 50th CV corresponding to the sample obtained at -0.5 mA cm⁻² for 1600 s (i.e., the best performing HER catalyst). It can be seen that the electrocatalytic activity starts to slightly fade from the 10th cycle, although the loss is not pronounced. The broad oxidation band recorded ca. -0.95 V corresponds to the oxidation of H₂ adsorbed onto the catalyst. In order to reveal possible changes on NP morphology and composition, FE-SEM images were taken after the HER tests (Fig. 13). No big changes in NP morphology were noticed when comparing the images before and after the HER experiments. The chemical composition remained the same although the density of NPs seemingly diminished a little bit. Stability was also assessed by means of chronoamperometry at -1.1 V (inset of Fig. 12). A reduction of 35% of the current density was observed after holding the potential for 2 h. The previously observed decrease of NP density can partly explain such apparent decrease in the catalytic activity. Nevertheless, the loss is not pronounced and an increase in the electrocatalytic activity was indeed observed in some cases (Fig. S9). Therefore, the here-developed substrate-supported Rh-Fe NPs hold promise in hydrogen production.

Finally, the HER activity of Rh-Fe NPs obtained at -0.5 , -2 and -4 mA cm⁻² but longer deposition times (3200 s) show a declined electrocatalytic activity (Fig. 14) probably due to an exceedingly large coverage and concomitant decrease of the surface area. In fact, the samples obtained under these conditions show bigger particles (Fig. 15). Deposits feature more than one layer of NPs (see for instance Fig. 15c) so that one can refer to them as ‘nanoparticulate films’. This result puts forward the importance of high surface area for enhancing HER activity.

3. Conclusions

Rh and Fe can be successfully co-deposited in the form of NPs by means of a low-cost method directly on a substrate. NPs showing tunable composition and size have been obtained by galvanostatic electrodeposition from the same electrolyte formulation. Relatively narrow particle size distributions were obtained within the studied range of current densities and up to 1600 s of deposition time. Larger deposition times render nanoparticulate-like films. The Fe content could be increased from 15 at% to 36 at% by increasing the applied current density. In this way, Rh can be partially replaced by a more abundant and less expensive element like Fe. XPS measurements are consistent with the presence of mainly metallic NPs. The electrocatalytic activity toward HER has been assessed in alkaline media with good results. Tunable HER performance has been observed depending on the electrodeposition conditions utilized to grow the NPs. The present work indicates that electrodeposition is a convenient method to prepare substrate-supported Rh-Fe based NPs for hydrogen production.

Supplementary data

FE-SEM images of NPs, histograms and CV curves.

Acknowledgements

This work has been partially funded by the 2014-SGR-1015 project from the Generalitat de Catalunya, the MAT2014-57960-C3-1-R from the Spanish Ministerio de Economía y Competitividad (MINECO), and by L'Oréal-Unesco through the 9th Edition of Spanish 'For Women in Science' and 2015 edition of 'International Rising Talents' programmes (awarded to Dr. Pellicer). Dr. Eva Pellicer is also grateful to MINECO for the "Ramon y Cajal" contract (RYC-2012-10839). Dr. Salvador Pané acknowledges financial support by the European Research Council Starting Grant "Magnetoelectric Chemonanorobotics for Chemical and Biomedical Applications (ELECTROCHEMBOTS)", by the ERC grant agreement no. 336456. Prof. Jordi Sort acknowledges the Consolidator Grant "Merging nanoporous materials with energy-efficient spintronics (SPIN-PORICS)" (Grant Agreement n_ 648454) from the European Research Council.

References

- [1] Nanoscale Materials (eds L. M. Liz-Marzán, P. V. Kamat), Kluwer Academic Publishers, Springer, 2003.
- [2] J. M. Pingarrón, P. Yáñez-Sedeño, A. González-Cortés, Gold nanoparticle-based electrochemical biosensors, *Electrochim. Acta* 53 (2008) 5848–5866.
- [3] H. Wei, Plasmonic silver nanoparticles for energy and optoelectronic applications, in *Advances in Nanomaterials and Nanostructures*, vol. 229 (eds K. Lu, N. Manjooran, M. Radovic, E. Medvedovski, E. A. Olevsky, C. Li, G. Singh, N. Chopra and G. Pickrell), John Wiley & Sons, Inc., Hoboken, NJ, USA, 2011.
- [4] M. Estrader, A. López-Ortega, S. Estradé, I. V. Golosovsky, G. Salazar-Alvarez, M. Vasilakaki, K. N. Trohidou, M. Varela, D. C. Stanley, M. Sinko, M. J. Pechan, D. J. Keavney, F. Peiró, S. Suriñach, M. D. Baró, J. Nogués, Robust antiferromagnetic coupling in hard-soft bi-magnetic core/shell nanoparticles, *Nature Commun.* 4 (2013) 2960.
- [5] P. He, H. Liu, Z. Li, Y. Liu, X. Xu, J. Li, Electrochemical deposition of silver in room-temperature ionic liquids and its surface-enhanced raman scattering effect, *Langmuir* 20 (2004) 10260-10267.
- [6] D. Zhang, W. C. Chang, T. Okajima, T. Ohsaka, Electrodeposition of platinum nanoparticles in a room-temperature ionic liquid, *Langmuir* 27 (2011) 14662-14668.
- [7] B. Özkale, E. Pellicer, M. A. Zeeshan, J. F. López-Barberá, J. Nogués, J. Sort, B. J. Nelson, S. Pané, One-pot electrosynthesis of multi-layered magnetic metallopolymer nanocomposites, *Nanoscale* 6 (2014) 4683-4690.

- [8] M. S. El-Deab, On the preferential crystallographic orientation of Au nanoparticles: effect of electrodeposition time, *Electrochim. Acta* 54 (2009) 3720–3725.
- [9] Y.-X. Chen, S.-P. Chen, Z.-Y. Zhou, N. Tian, Y.-X. Jiang, S.-G. Sun, Y. Ding, Z. L. Wang, Tuning the shape and catalytic activity of Fe nanocrystals from rhombic dodecahedra and tetragonal bipyramids to cubes by electrochemistry, *J. Am. Chem. Soc.* 131 (2009) 10860–10862.
- [10] Y. Li, P. Diao, T. Jin, J. Sun, D. Xu, Shape-controlled electrodeposition of standing Rh nanoplates on indium tin oxide substrates and their electrocatalytic activity toward formic acid oxidation, *Electrochim. Acta* 83 (2012) 146–154.
- [11] J. Schulz, A. Roucoux, H. Patin, Unprecedented efficient hydrogenation of arenes in biphasic liquid–liquid catalysis by re-usable aqueous colloidal suspensions of rhodium, *Chem. Commun.* (1999) 535.
- [12] Y. Motoyama, M. Takasaki, S. H. Yoon, I. Mochida, H. Nagashima, Rhodium nanoparticles supported on carbon nanofibers as an arene hydrogenation catalyst highly tolerant to a coexisting epoxido group, *Org. Lett.* (11) 2009 5042–5045.
- [13] J. M. Ziegelbauer, D. Gatewood, F. Gullá, J. F. Andrea, M. Guinel, F. Ernst, D. E. Ramaker, S. Mukerjee, Fundamental investigation of oxygen reduction reaction on rhodium sulfide-based chalcogenides, *J. Phys. Chem. C* 113 (2009) 6955–6968.
- [14] H. Lam-Wing, M. J. Weaver, Adsorption and electrooxidation of some simple organic molecules on rhodium(111) as probed by real-time FTIR spectroscopy: Comparisons with platinum (111), *J. Phys. Chem.* (93) 1989 7218–7226.

- [15] B. R. Sathe, High aspect ratio rhodium nanostructures for tunable electrocatalytic performance, *Phys. Chem. Chem. Phys.* 15 (2013) 7866-7872.
- [16] M. Doyle, G. Rajendran, *Handbook of Fuel Cells Fundamentals, Technology and Applications*, John Wiley & Sons, Chichester, U. K., 2003.
- [17] M. A. Haider, M. R. Gogate, R. J. Davis, Fe-promotion of supported Rh catalysts for direct conversion of syngas to ethanol, *J. Catal.* 261 (2009) 9-16.
- [18] I. Nakamura, Y. Yamanoi, T. Imaoka, K. Yamamoto, H. Nishihara, A uniform bimetallic rhodium/iron nanoparticle catalyst for the hydrogenation of olefins and nitroarenes, *Angew. Chem.* 123 (2011) 5952-5955.
- [19] F. Safizadeh, E. Ghali, G. Houlachi, Electrocatalysis developments for hydrogen evolution reaction in alkaline solutions – A review, *Int. Hydrog. Energy* 40 (2015) 256-274.
- [20] Y. Zheng, Y. Jiao, M. Jaroniec, S.Z. Qiao, Advancing the electrochemistry of the hydrogen-evolution reaction through combining experiment and theory, *Angew. Chem. Int. Ed.* 54 (2015) 52-65.
- [21] P. K. Wrona, A. Lasia, M. Lessard, H. Ménard, Kinetics of the hydrogen evolution reaction on a rhodium electrode, *Electrochim. Acta* 37 (1992) 1283-1294.
- [22] R. Palaniappan, D. C. Ingram, G. G. Botte, Hydrogen evolution reaction kinetics on electrodeposited Pt-M (M = Ir, Ru, Rh, and Ni) cathodes for ammonia electrolysis electrochemical engineering, *J. Electrochem. Soc.* 161 (2004) E12-E22.
- [23] M. Smiljanic, Z. Rakocevic, A. Maksic, S. Strbac, Hydrogen evolution reaction on platinum catalyzed by palladium and rhodium nanoislands, *Electrochim. Acta* 117 (2014) 336-343.

- [24] J.-R. McKone, S.-C. Marinescu, B. S. Brunschwig, J. R. Winkler, H. B. Gray, Earth-abundant hydrogen evolution electrocatalysts, *Chem. Sci.* 5 (2014) 865-878.
- [25] R. Subbaraman, D. Tripkovic, K.-C. Chang, D. Strmcnik, A. P. Paulikas, P. Hirunsit, M. Chan, J. Greeley, V. Stamenkovic, N. M. Markovic, Trends in activity for the water electrolyser reactions on 3d M(Ni,Co,Fe,Mn) hydr(oxy)oxide catalysts, *Nature Mater.* 11 (2012) 550-557.
- [26] A. T. Miller, B. L. Hassler, G. G. Botte, Rhodium electrodeposition on nickel electrodes used for urea electrolysis *J. Appl. Electrochem.* 42 (2012) 925-934.
- [27] S.-H. Son, H.-K. Lee and S.-C. Park, Kinetics of rhodium electrodeposition for semiconductor interconnect applications, *Surf. Interface Anal.* 42 (2012) 1244-1246.
- [28] M. Izaki, Electrodeposition of Iron and Iron alloys, in *Modern electroplating*, Fifth edition, (eds M. Schlesinger and M. Paunovic), John Wiley & Sons, Inc., Hoboken, NJ, USA, 2010.
- [29] R. D. Noce, A. V. Benedetti, E. C. Passamani, H. Kumar, D. R. Cornejo, M. Magnani, Use of conventional electrochemical techniques to produce crystalline FeRh alloys induced by Ag seed layer, *J. Alloys Compd.* 573 (2013) 37-42.
- [30] S. Salem-Sugui Jr., A. D. Alvarenga, R. D. Noce, R. B. Guimarães, C. Salazar Mejia, H. Salim, F. G. Gandra, Anomalous metamagnetic-like transition in a FeRh/Fe₃Pt interface occurring at $T \approx 120$ K in the field-cooled-cooling curves for low magnetic fields, *AIP Adv.* 2 (2012) 032168.
- [31] *Electrochemical Production of Metal Powders* (ed S. S. Djokić), Springer, 2012, p. 281

- [32] I. Tabakovic, S. Riemer, V. Vas'ko, M. Kief, CoFeRh alloys: Part 2. Electrodeposition of CoFeRh alloys with high saturation magnetic flux density and high corrosion resistance, *Electrochim. Acta* 53 (2008) 8008-8014.
- [33] K. Mech, P. Żabiński, R. Kowalik, Analysis of rhodium electrodeposition from chloride solutions electrochemical/electroless deposition, *J. Electrochem. Soc.* 161 (2014) D458-D461.
- [34] S. Langerock, L. Heerman. Study of the electrodeposition of rhodium on polycrystalline gold electrodes by quartz microbalance and voltammetric techniques, *J. Electrochem. Soc.* 151 (2004) C155-C160.
- [35] Y. M. Wang, S. Cheng, Q.M. Wei, E. Ma, T.G. Nieh, A. Hamza, Effects of annealing and impurities on tensile properties of electrodeposited nanocrystalline Ni, *Scripta Mater.* 51 (2004) 1023-1028.
- [36] <http://xpsimplified.com/elements/rhodium.php>
- [37] I. Tabakovic, J.-M. Qiu, S. Riemer, M. Sun, V. Vas'ko and M. Kief, CoFeRh alloys: Part 1. Electrodeposition of Rh and nonmagnetic CoFeRh alloy, *Electrochim. Acta* 53 (2008) 2483-2493.
- [38] Handbook of Surfaces and Interfaces of Materials, Five-Volume Set (eds Hari Singh Nalwa), Academic Press, 2001, pp. 566-567.
- [39] S. Suzuki, K. Sugiyama, Y. Waseda. Changes in the chemical state and composition of the surface of iron oxides due to argon ion sputtering, *J. Surf. Anal.* 9 (2002) 455-458.
- [40] C. S. Tiwary, S. Kashyap, K. Biswas, K. Chattopadhyay, Synthesis of pure iron magnetic nanoparticles in large quantity, *J. Phys. D: Appl. Phys.* 46 (2013) 385001.

[41] L. A. Kibler, M. Kleinert, D. M. Kolb, The initial stages of rhodium deposition on Au(111), J. Electroanal. Chem. 467 (1999) 249-257.

Figure captions

Figure 1. Representative E-t transients for NPs deposition onto Au/Ti/Si substrates at the indicated current densities.

Figure 2. FE-SEM images of NPs obtained at fixed deposition charge: (a, b) $j = -0.5 \text{ mA cm}^{-2}$, 1600 s, (c, d) $j = -2 \text{ mA cm}^{-2}$, 400 s and (e, f) $j = -4 \text{ mA cm}^{-2}$, 200 s.

Figure 3. FE-SEM images of NPs obtained at $j = -0.5 \text{ mA cm}^{-2}$ for different deposition times (3200, 1600 and 800 s). Magnification is the same for both the large SEM images and the insets. Scale bar is the same for all images (and insets).

Figure 4. Representative EDX patterns corresponding to NPs obtained at (a) $j = -0.5 \text{ mA cm}^{-2}$ for 1600 s and (b) $j = -4 \text{ mA cm}^{-2}$ for 200 s.

Figure 5. (a) XPS survey spectrum and detail of (b) Rh3d, Fe2p and O1s regions (before 1 min Ar sputtering) for NPs fabricated at -0.5 mA cm^{-2} for 1600s.

Figure 6. (a) XPS survey spectrum and detail of (b) Rh3d, Fe2p and O1s regions (after 1 min Ar sputtering) for NPs fabricated at -0.5 mA cm^{-2} for 1600s.

Figure 7. (a) TEM and (b) HRTEM images and (c) SAED pattern of NPs obtained at -0.5 mA cm^{-2} for 1600 s.

Figure 8. (a) TEM, (b) STEM images and (c) EDX line scan of a Rh-Fe NP obtained at -0.5 mA cm^{-2} for 1600 s. Mean Fe content is 15 at%, in agreement with Table 1.

Figure 9. LSV curves in 0.1 M NaOH (50 mV s^{-1}) of Rh-Fe NPs obtained at different current densities and deposition times.

Figure 10. SEM image of (a) pure Rh NPs electrodeposited at -0.5 mA cm^{-2} for 1600 s from an Fe-free bath containing 0.5 mM $\text{Cl}_6\text{Na}_3\text{Rh}$ + 0.05 M glycine + 0.05 M NaCl (pH = 2.4) and b) pure Fe electrodeposited at -4 mA cm^{-2} for 1600 s from a Rh-free bath containing 0.01 M FeCl_3 + 0.05 M glycine + 0.05 M NaCl (pH = 2.4). Scale bar is the same for both images.

Figure 11. LSV curves in 0.1 M NaOH (50 mV s^{-1}) of bare Au surface (Si/Ti/Au substrate), pure Rh and pure Fe materials, and the outperforming Rh-Fe NPs (at the indicated current density and deposition time).

Figure 12. CV curves in 0.1 M NaOH (50 mV s^{-1}) of Rh-Fe NPs obtained at $j = -0.5 \text{ mA cm}^{-2}$ and 1600 s. The inset shows the j vs. t curve for an applied potential of -1.1 V .

Figure 13. FE-SEM images taken before and after 50 CV cycles of Rh-Fe NPs obtained at $j = -0.5 \text{ mA cm}^{-2}$ for 1600s.

Figure 14. LSV curves 0.1 M NaOH (50 mV s^{-1}) of Rh-Fe NPs obtained at different current densities and fixed long deposition time (3200 s).

Figure 15. FE-SEM images of NPs obtained at (a) $j = -0.5 \text{ mA cm}^{-2}$, (b) -2 mA cm^{-2} and (c) -4 mA cm^{-2} for 3200 s of deposition time. Scale bar is the same for all images.

Table 1. Mean size (\pm standard deviation) of the NPs as a function of the applied current density and deposition time.

		Mean size (\pm nm)		
$-j$ (mA cm ⁻²)		0.5	2	4
time (s)	200	31.4 \pm 7.1	24.5 \pm 4.3	22.5 \pm 3.4
	400	41.1 \pm 9.3	48.2 \pm 8.5	29.8 \pm 5.5
	800	37.8 \pm 5.6	41.5 \pm 7.8	49.2 \pm 8.3
	1600	42.7 \pm 11.1	52.3 \pm 8.9	49.0 \pm 6.6
	3200	58.3 \pm 13.4	76.6 \pm 12.8	81.2 \pm 18.8

Table 2. Fe content (at%) determined by EDX in NPs grown at different current densities and deposition times. Oxygen was excluded before normalization. The standard deviation is ± 2 -5 at%.

$-j$ (mA cm ⁻²)	at% Fe				
	$t = 200$ s	$t = 400$	$t = 800$	$t = 1600$	$t = 3200$
0.5	N/A	N/A	15	19	21
2	N/A	28	14	16	17
4	N/A	32	36	31	25

*N/A: Conditions leading to the smallest nanoparticles and/or the lowest coverage. The associated Fe amounts are not reported because they have high associated error.

Table 3. Rh, Fe and O content in the NPs as determined by XPS both before and after Ar ions sputtering for NPs fabricated at -0.5 mA cm^{-2} at 1600s.

	at% Rh	at% Fe	at% O
before Ar ions sputtering	11	19	70
after Ar ions sputtering	86	14	<1

Table 4. Onset potential for HER and current density at -1.2 V for NPs deposited at different electrodeposition conditions. Values are extracted from the LSV curves shown in Fig. 8.

Electrodeposition conditions	Onset potential for HER	$-j / \text{mA cm}^{-2}$
	/ V	at $E = -1.2$ V
-0.5 mA cm^{-2} , 1600 s	-0.93	15.0
-2 mA cm^{-2} , 400 s	-0.95	4.7
-2 mA cm^{-2} , 1600 s	-0.95	12.2
-4 mA cm^{-2} , 200 s	-0.96	4.1
-4 mA cm^{-2} , 800 s	-0.94	8.4